Postprint of: Bilal M., Lopez-Aguayo S., Szczerska M., Madni H., Multi-functional sensor based on photonic crystal fiber using plasmonic material and magnetic fluid, OSA Continuum Vol. 61, Iss. 35 (2022), pp. 10400-10407, DOI: 10.1364/optcon.456519

Multi-functional sensor based on photonic crystal fiber using plasmonic material and magnetic fluid

Muhammad Musavir Bilal,[1,2,5] Servando López-Aguayo,[1,*] Małgorzata Szczerska,[2,6] and Hamza Ahmad Madni[3,4,7]

[1] *Tecnológico de Monterrey, Escuela de Ingeniería y Ciencias, Ave. Eugenio Garza Sada 2501, Monterrey, N.L. 64849, México.*
[2] *Department of Metrology and Optoelectronics, Faculty of Electronics, Telecommunications and Informatics, Gdańsk University of Technology, 11/12 Narutowicza Street,80-233 Gdańsk, Poland.*
[3] *Faculty of Electronics, Telecommunications and Informatics, Gdańsk University of Technology, 80-233 Gdansk, Poland.*
[4] *Department of Computer Engineering, Khwaja Fareed University of Engineering Information Technology, Rahim Yar Khan, 64200, Pakistan.*
[5] *A00829594@tec.mx*
[6] *malszcze@pg.edu.pl*
[7] *101101770@seu.edu.cn*
* *servando@tec.mx*

Abstract: A unique highly sensitive photonic crystal fiber is investigated based on plasmonic material and magnetic fluid (MF) for the simultaneous measurement of temperature and magnetic field sensor. The designed sensor is explored by tracing the different parameters such as birefringence, coupling length, power spectrum, and the peak wavelength of the transmission intensity. The magnetic field and temperature computation are attained simultaneously by examining the linear fitting curve and the movement of transmission peaks. The obtained sensitivity for temperature is 7.1nm/°C with an exposure range of 25°C to 100°C. In contrast, the magnetic field sensitivity is 12nm/Oe with a detection range of 160-200 Oe. In addition, the resolutions are -1.245°C, 5.53 Oe for temperature and magnetic field, respectively. Our inspected sensor is used to detect extremely low and high values of magnetic fields. The investigated structure is presented with simplification, compactness, easy implementation, and high sensitivity, which is expected to be a good foundation for the advancement of optical sensing devices in the future applications of industries, security, small grids, and environmental systems.

1. Introduction

The surface plasmon resonance (SPR)-based sensing technique has been revealed tremendous attention for its sensitivity to diverse applications in the fields of chemical sensing, biosensing, and environmental monitoring [1]. SPR is an optical circumstance happening when an electromagnetic impulse is produced in the metal surface due to the interface among optical electromagnetic fields and free electrons of the metal. It creates the stimulation of the surface plasmon polaritons (SPPs) spreading at the conductor-dielectric interface. The surface plasmons are extremely sensitive to the surrounding refractive index (RI), which is suitable for optical sensing applications [2,3]. There are many opportunities related to the SPR perception, which have been authorized to develop a wide variety of sensors that allocate outstanding features such as high resolution and a wide range of sensitivity. Furthermore, the linkage of optical fiber sensors with plasmonic materials adds some new and exciting features to their remarkable performance of real-time measurements, multiplexing, and the possibility of

developing all-fiber systems for remote sensing. SPR sensors have become a research hotspot because of their potential applications [4,5].

In the past, the prism-based SPR method was used. SPR sensors based on prism technology like slot waveguide and v-groove waveguide have been studied. However, the prism-based surface plasmon sensor structure is immense, complicated, and expensive because of optical and mechanical elements that are not appropriate for remote sensing [6].

Photonic crystal fiber (PCF) is a modern kind of microstructure optical fiber consisting of the fiber core, cladding, and metal nanowires in the air hole. The visual function of the PCF can be reformed by enhancing the periodic layout of the air holes of the fiber cladding, the size of the air holes, and the form of metal nanowire [7]. In contrast with the traditional optical fibers, combining the SPR technology with the PCF has been widely studied in the sensing fields due to their advantages of reliability, stability, small size, remote sensing ability, immunity to electromagnetic intervention, and extensive range of environmental monitoring [8]. On the other hand, instantaneous detection of the magnetic field and temperature is crucial for industrial applications. The accurate measurement of multi-parameters is almost complex due to the cross-sensitivity effect. Therefore, different functional plasmonic materials and liquids are added into the cladding or core region of the PCF to detect more than one parameter. Generally, silver, copper, gold, and aluminum are utilized as plasmonic materials. In recent years, gold and silver have become a hot topic for PCF-SPR based sensor techniques, but the performance and the measurement accuracy of silver material have been reduced due to the oxidation problem [9].

Therefore, gold delivers higher sensitivity while encountering the physical parameters. The high refractive index analyte-like magnetic fluid can be used for magnetic field sensing. As it is well known, the behaviors of ferromagnetic particles rely on both the external temperature and the applied magnetic field strength. The refractive index properties could be exploited as the imaginary basement to acquire the real-time detection of the magnetic field and temperature [10]. Recently, many researchers studied the surface plasmon resonance technology based on the photonic crystal fiber for sensing the different parameters and disposed the characteristics of the structure. The measurement of single parameters has been analyzed based on the photonic crystal fiber by utilizing the plasmonic materials and highly refractive index analytes [11,12]. In 2012, the surface plasmon resonances based on the PCF for the temperature measurement has been designed [13]. The simultaneous measurement of temperature and magnetic field based on cascaded photonic crystal fibers with surface plasmon resonance has been investigated [14]. Moreover, the D-shaped photonic crystal fiber (PCF) sensor based on the plasmonic effect and Sagnac interference technology has been constructed for measuring the magnetic field and temperature [15]. Similarly, the photonic crystal fiber-based magnetic fluid and FBG for magnetic field and temperature sensing came to exist [16] Meanwhile, it has been observed that the previous designs have more complex geometries (such as dual-core PCF, D-shape PCF, and cascaded PCF) which may create hurdles in the fabrication process and make it costly. Moreover, in the previous works, the single sensing, and multifunctional sensing materials have been investigated to measure the physical parameters, but a need still exists to improve the sensitivity with simple geometric structure at low cost and easiness.

In this study, a photonic crystal fiber based on the plasmonic material and magnetic fluid has been exploited for the simultaneous measurement of temperature and magnetic field. The effective plasmonic material and sensing fluid are employed at the center of the PCF, which reduces the construction challenges. In contrast with the previously designed plasmonic material devices that work on transmission loss, our designed structure works based on the effective refractive index, birefringence, coupling length, power, and transmission spectrum attributes by utilizing the finite element method (FEM). The parameters of the designed structure are appropriately modified to achieve the best sensitivity of the proposed model. The achieved sensitivities are 12nm/Oe and 7.1nm/^{o}C for magnetic field and temperature,

respectively. Furthermore, the figure of merit (FOM) and resolution for the proposed sensor have been calculated which is 665 Oe and 5.53 Oe, respectively. Our theoretical results are supported by a simulations study based on the COMSOL multiphysics software.

2. Design and fabrication

The geometrical structure of the photonic crystal fiber based on the plasmonic material is shown in Fig. 1. The cladding region is arranged with the air holes, and the size of each air hole is denoted by d (0.4μm). The distance between two adjacent air holes is expressed with pitch Λ (0.60μm). The core region consists of the four air holes surrounded by a gold layer and is mentioned with D (1.46μm). The core region is filled with magnetic fluid except for the air holes. The interaction of MF and plasmonic material leads to causes the external sensing schemes. A thin layer of gold is coated as a plasmonic material around the fiber that is chemically stable, has high-quality peak shifts, and it has less possibility of getting oxidized in the existence of fluid sensing mode. The thickness of the gold layer is mentioned with t_g (30nm). The outer layer contains a perfectly matched layer (PML). PML is manipulated to absorb radiant energy, which incident at several angles. All the sensor parameters are considered in such a way for better performance.

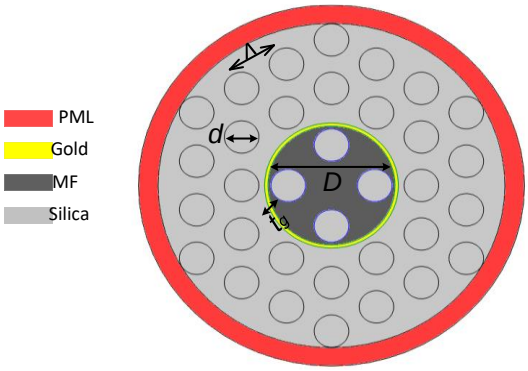

Fig. 1. The geometrical structure of the proposed PCF.

The advantage of this type of fiber is a simple structure in manufacturing, and more air holes enclosed to the center enhance the less leakage of light. The designed geometry can be fabricated by applying a high-temperature furnace in a standard fiber drawing tower. After formulating fiber preform, silica rods and capillaries are assembled together using stack and draw technique [17]. Moreover, the fabrication process of the proposed structure and steps involved in designing have been shown in Fig. 2.

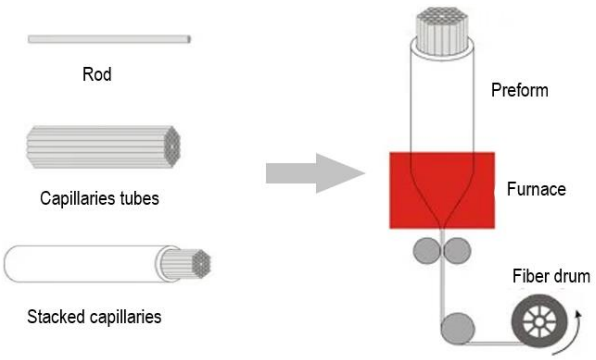

Fig. 2. Fabrication Process of the proposed structure.

Combining the gold layer with PCF is a crucial matter that requires high temperature in some deposition techniques like radio frequency, sputtering and thermal evaporation. Moreover, chemical vapor deposition (CVD) is the most common and popular method that can be exploited to deposit the gold layer effectively [18].

3. Materials and method

In the proposed structure, cladding region mostly consists of air holes with a refractive index of 1, and silica is used as background material in the remaining parts of the cladding area. The Sellmeier equation is applied to calculate the refractive index of silica. MF is a water-based liquid consisting of ferromagnetic nanoparticles that are highly influenced by the external magnetic field. Thus, changes in the refractive index of the MF lead to the shift in optical properties. Therefore, the output spectrum of the fiber mode interferometer fluctuates due to the interference between the evanescent mode field and the sensing material.

Moreover, the performances of ferromagnetic particles are dependent on both the external temperature and applied magnetic field [19]. The tunable RI feature can be used to attain the simultaneous measurement of temperature and magnetic field. Whereas the refractive index of the magnetic fluid can be defined as a function of temperature and external magnetic field by using the empirical equation of the Langevin method [20].

$$n_{MF} = [n_m - n_0]\left[coth\left(a\frac{H-H_{c,n}}{T}\right) - \frac{T}{a(H-H_{c,n})}\right] + n_0, \quad (1)$$

where $H_{c,n}$ is the critical field intensity, after which the refractive index n starts to change. n_o is the refractive index of MF when the magnetic field H is lower than $H_{c,n}$. n_m is the saturated value of the refractive index. T denotes the temperature of MF. a is the fitting parameter. Next, the gold layer enhances the detection capability of the sensor. The material dispersion of *Au* to achieve the dielectric function is characterized by the Drude-Lorentz model [21].

$$\mathcal{E}_{Au} = \mathcal{E}_\infty - \frac{\omega_D^2}{\omega(\omega + j\gamma_D)} - \frac{\Delta\varepsilon.\Omega_L^2}{(\omega^2 - \Omega_L^2) + j\Gamma_L\omega}, \quad (2)$$

where ε_{Au} is the permittivity of gold, ε_∞ = 5.9673 is the permittivity of gold at high frequency, $\omega = 2\pi c/\lambda$ is known as the angular frequency where c is the velocity of light, ω_D = 2113.6 *THz* × 2π is known as plasma frequency, γ_D = 15.92 *THz* is known as damping frequency and $\Delta\varepsilon$ = 1.09 is denoted by the weighting factor. Ω_L= 650.07 × 2π *THz* and Γ_L =104.86 × 2π *THz* are known as Lorentz oscillator strength and spectral width, respectively.

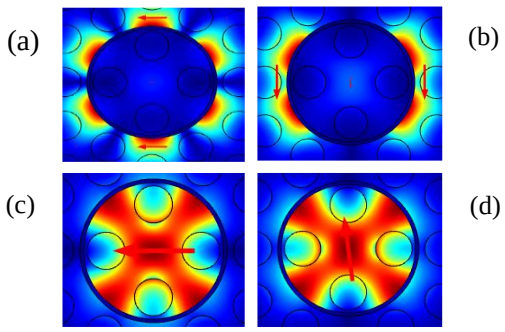

Fig. 3. Electric field distribution of proposed sensor, SPP mode: (a) X- and (b) Y-polarization; fundamental mode: (c) X- and (d) Y-polarization, red arrows indicate the direction of light.

Finite element method (FEM) based on COMSOL multiphysics software is manipulated to fabricate and evaluate the spreading mode of the proposed sensor. In computation, the physics-controlled way of the meshing system is studied, and the more acceptable method of mesh size is selected for better simulation results. Fig. 3(a,b) indicates the phenomena of light

transmission of SPP mode for *X* and *Y* polarization. Arrows indicated the direction of lights. It can be clearly seen that the light is totally enclosed at the metal surface. SPP mode is an electromagnetic excitation at the metal layer to display the resonance at the plasmonic surface. On the other hand, Fig. 3(c,d) shows the core guided mode in which the light is strongly confined at the center of the PCF due to the high refractive index of the magnetic fluid.

Fig. 4 shows the dispersion of the light spectrum between the fundamental mode and SPP mode. In this graph, the effective index of the real part is taken from the left side and confinement loss from the right side. The black solid and dotted lines show the core and SPP mode variation, respectively. The red line shows the loss curve. It has been seen that at the wavelength of 1.5μm, the phase matching point occurred. At this point, the light is shifted from SPP mode to fundamental mode, where the maximum loss has been observed. Usually, SPP mode operates at visible radiation and fundamental mode operates at infrared radiation. Due to the combination of analytes (MF) with a high refractive index of plasmonic material, the resonance wavelength is received at 1.5μm (IR) band as the energy is transferred from SPP mode to fundamental mode. The effective refractive index (n_{eff}) for core and SPP mode is gradually decreased with the increase of wavelength. So, at the minimum wavelength, a higher refractive index is achieved for X-polarization. A similar mechanism also happens for the Y-polarized core-guided mode. But it illustrates the low loss intensity as compared to the X-polarized core-guided mode. Due to the high intensity of the magnetic fluid and more confinement of light, only the X-polarized core-guided mode is counted to assess the sensor schemes.

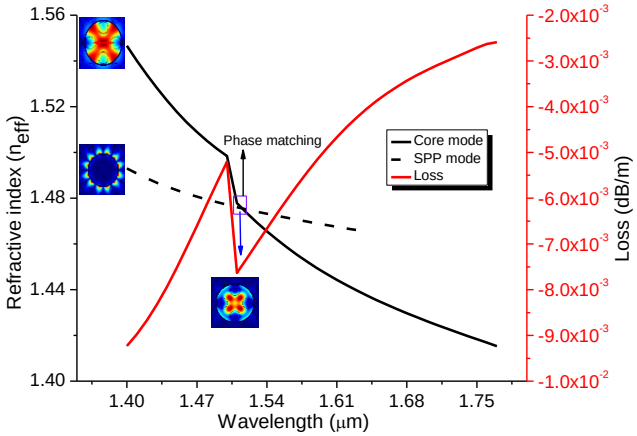

Fig. 4. Dispersion relation of the core guided and SPP mode.

In this simulation study, energy coupling changes its position from the core mode to the surface plasmon polarization (SPP) mode. The highest loss occurs at the resonance wavelength. Basically, the calculation and discussions of the proposed PCF have been analyzed based on the birefringence, coupling length, power spectrum, and transmission intensity, whereas the confinement loss (CL) is the critical factor in assessing the performance of the sensor. The following equation analyzes the model loss in dB/m of the fundamental core guided mode [22,23].

$$CL\left(\frac{dB}{m}\right) = 8.686 \times \left(\frac{2\pi}{\lambda}\right) \times Im\left[n_{eff}\right] \times 10^{6}, \tag{3}$$

The mechanism of confinement loss spectrum for *X* polarization core mode has been shown in Fig. 5. After applying the external magnetic field strength, a peak loss curve has appeared at the specific wavelength (1.53μm) due to the influence of light with the change of the refractive index. It has been seen that as the magnetic field is increased, the loss curve is also increased

regarding the wavelength. Additionally, at the maximum magnetic field strength, the loss will be higher. After that, there is a linear curve occurred from the wavelength of 1.54μm to 1.8μm.

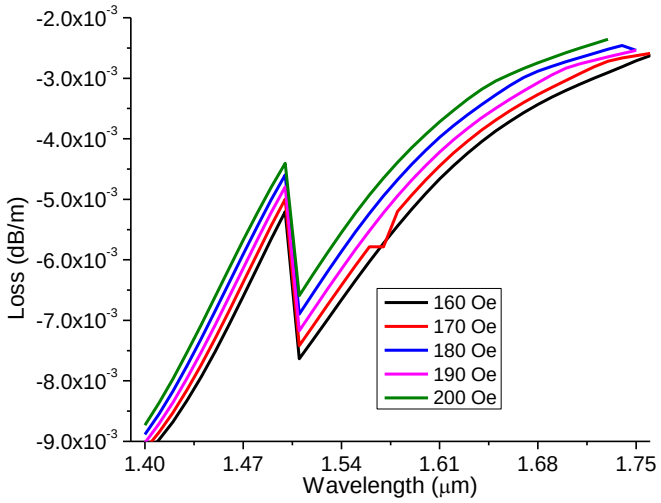

Fig. 5. The loss spectrum concerning with magnetic field.

4. Results and Discussions

In this model, for the whole process, the operating wavelength is taken from 1.6μm to 2.1μm. The light spectrum between the *X* and *Y* polarization generates interference at a different wavelength by applying the external parameters. This interference relates to the change of the effective refractive index. The effective refractive index difference between the *X* and *Y* polarization beams of light results in an optical phase difference. Filling the MF solution into the center of the PCF reduces the effective refractive index. The low refractive index difference is reliable for high sensitivity. Birefringence can be evaluated by using the following equation [24] .

$$B = |n_x - n_y|, \tag{4}$$

where B is the birefringence, n_x and n_y are the differences in effective refractive index.

The intended sensor works based on the light intensity modulation. It is recognized that the refractive index of the PCF background material (Silica) is not responsive to the magnetic field. However, the casually consistent structure of magnetic particles changes under an external magnetic field. Therefore, the relocation of Fe_3O_4 nanoparticles leads to the refractive index deviation accordingly. Commonly, n_{eff} increases with the magnetic field, which causes the shift of peaks and dips of the proposed structure [25].

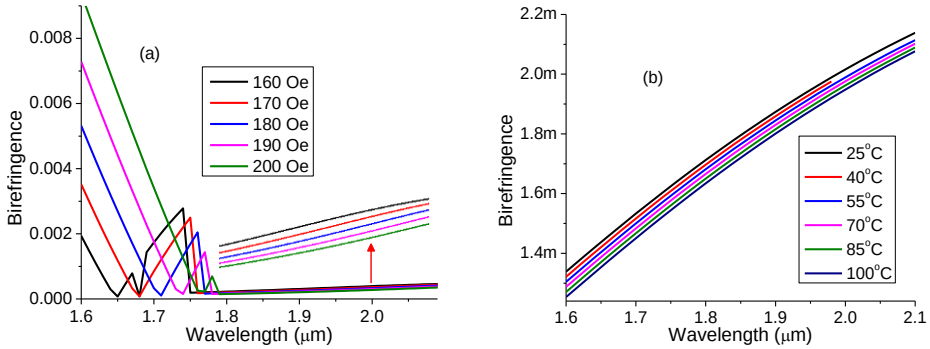

Fig. 6. The variation between the birefringence and wavelength by applied a) magnetic field and b) temperature.

For sensing the magnetic field, the temperature has been kept constant at 25ºC. The variation between the birefringence and wavelength as a function of the external magnetic field has been shown in Fig. 6(a). The range of the applied magnetic field is from 160 Oe to 200 Oe. The measurement of the weak magnetic field has been analyzed before in many articles. In this simulation study, the maximum range has been taken which is 200 Oe after that, the wavelength shift of the designed sensor tends to be stable for the agglomerations saturations of magnetic particles [26].

At the minimum wavelength, the maximum birefringence is obtained. The peak spectrum has occurred at the wavelength of 1.75µm due to the effect of the magnetic fluid. Here, it has been noticed that as the external magnetic field increases, the birefringence and wavelength decrease. After that, there is a linear spectrum happened from 1.80µm to 2.1µm. Next, the temperature mechanism with respect to birefringence and wavelength has been shown in Fig. 6(b). This graph illustrates that there is a constant increment of birefringence with the increase of wavelength. By increasing the temperature, the birefringence is gradually decreased. The values of temperature are taken from 25ºC to 100ºC. In accordance with the need for applications in the real world, our chosen range of temperature is a bonus point to accept the validity of our work as it is the environmental temperature. Thus, our designed sensor is best for measuring ecological temperature. Another essential factor is known as coupling length, which influences the performance of the sensor. Coupling length is associated with birefringence, which can be measured by using the following equation [27].

$$L = \frac{\lambda}{2 \times B}, \tag{5}$$

Here L is the coupling length, λ is the operating wavelength, and B is the birefringence.

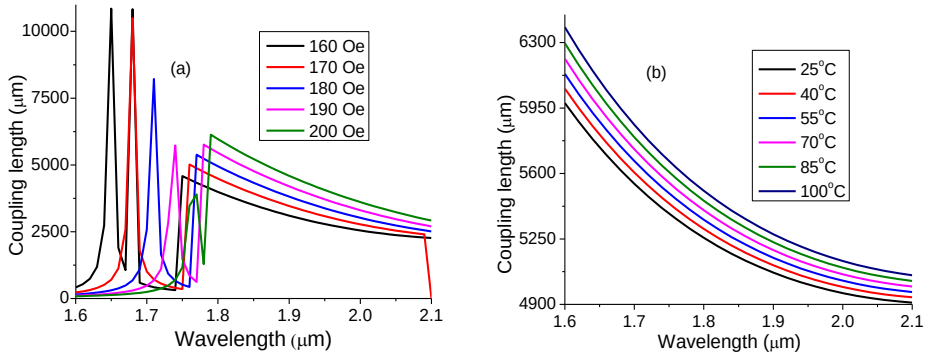

Fig. 7. The relationship of a coupling length and wavelength as a function of a) magnetic field and b) temperature.

Fig. 7(a) shows the relation between the coupling length and the operating wavelength as an external magnetic field function. This graph depicts the inverse reaction of the birefringence. At the beginning of wavelength, a dip spectrum has been observed by varying the outer magnetic field strength. Whereas, at the minimum magnetic field strength, the highest peak of coupling length has been realized and then gradually decreases as the magnetic field increases. After that, a constant light spectrum was received from the wavelength of 1.8µm to 2.1µm. It is viewed that with the

increasing of wavelength, the coupling length is slightly going to decrease. The same phenomenon is represented in Fig. 7(b) by applying the temperature, but no peak wavelength has been detected. Here, it is clearly shown that a linear spectrum has transpired between the wavelength and the coupling length. The maximum coupling length has been attained at the minimum wavelength and then steadily decreases by increasing the wavelength.

Based on the coupling-mode theory, the optical power changes from one mode to another, along with the proposed sensor. The term coupling length can describe the power spectrum as

it is highly associated with birefringence. The power spectrum ensures the sensor proficiency, which is determined by using the equation [28].

$$P(out) = sin^2\left(\frac{B\times\pi\times L}{\lambda}\right), \quad (6)$$

Where B is the birefringence, L is the coupling length, and λ is the operating wavelength.

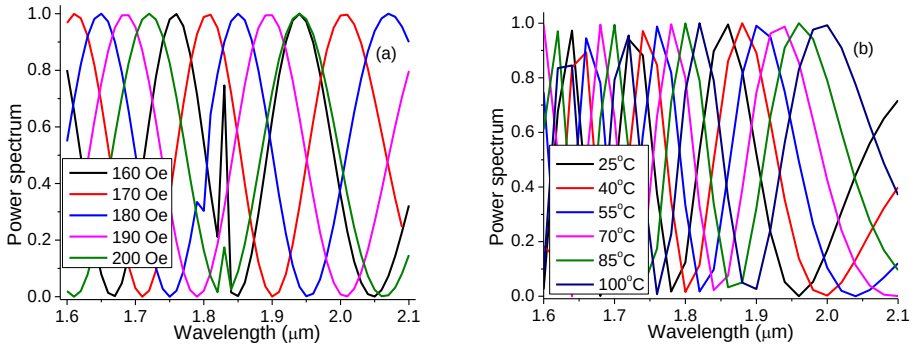

Fig. 8. The variation of the power spectrum to wavelength in terms of a) magnetic field and b) temperature.

At the maximum power spectrum, the peak wavelength shift is occurred by applying the external magnetic field strength has been shown in Fig. 8(a). Thus, the variation of light signals has been achieved between the wavelength and power spectrum. As the wavelength is increased, the shift of the power spectrum is moving at the maximum wavelength. On the other hand, the same phenomena have been found after applying the external temperature. Fig. 8(b) shows the peak shift which has been appeared at the maximum power spectrum. As the temperature is going to increases, the peak shift moves to a higher wavelength.

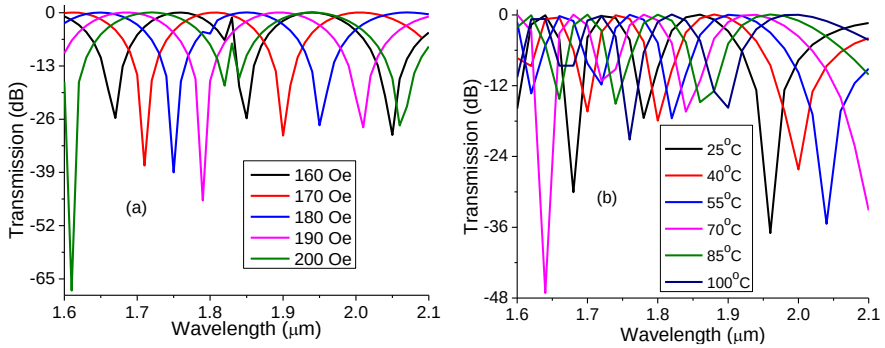

Fig. 9. Comparison of a transmission spectrum with a) magnetic field and b) temperature.

Additionally, the transmission spectrum is the significant parameter to calculate the sensitivity of the temperature and the magnetic field. The intensity modification of pulse propagation has been exploited. The overall plasmonic impact significantly varies on the transmittance. However, the wavelength sensitivity of the intended sensor can be computed through the shift of the sharp peak of the transmittance curve on a specific wavelength for the absolute deviation of the refractive index. The transmittance spectrum can be assessed by using the following equation [28].

$$T_r(dB) = 10 \times log_{10}\left(\frac{P_{out}}{P_{in}}\right), \quad (7)$$

where T_r (dB) is the transmittance spectrum, P_{out} and P_{in} are the maximum output and input power functions.

The comparison graph between transmission and wavelength as a serve of the external magnetic field has been shown in Fig. 9(a). When the external magnetic field is applied, different peak spectrums appear at different wavelengths. The transmittance outline fluctuates from 0dB to -70dB, displaying a solid descending peak for each value of external magnetic field strength. Furthermore, the maximum and minimum feasible transmittance outlines are -70dB, -25dB for 200 Oe, and 160 Oe magnetic field strength, respectively. Next, Fig. 9(b) shows the transmittance for the temperature 25ºC−100ºC. By varying the temperature, peak shift has been displayed at different wavelengths. The transmittance summary modifies from 0 to -50dB, illustrating a sharp downward climax for each value of applied temperature. The maximum transmission spectrum has been achieved at -49dB for the value of 70ºC.

Based on the beyond consequence, the correlation among peak shifts and variation of temperature and magnetic field has been depicted in Fig. 10(a) and (b), respectively. The linear response of the wavelength alteration with the applied magnetic field and temperature is exposed. The links of fitting curves are 0.99, signifying good linear connections. The best-matched regression line reveals the best execution with a highly linear reaction. According to Fig. 10, the variation of peak factors of the resonance wavelength precisely relies on the shift of phase difference, which is induced by the change of effective RI. The linear fitting functions of intercept and slope are 1, 0.0053, and 1.74, 0.0014 for magnetic field and temperature sensing, respectively.

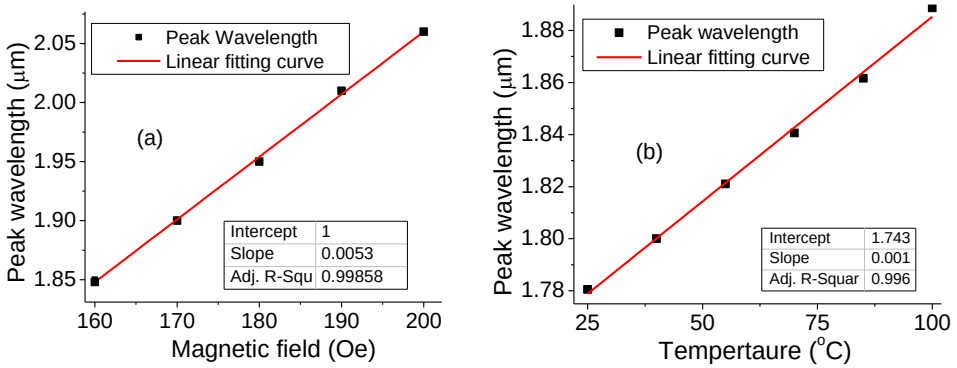

Fig. 10. The dip wavelength versus a) magnetic field and b) temperature effects.

Furthermore, the sensitivity rises and falls depending on the peak wavelength variation and the change of external parameters. The following equations can be employed to determine the sensitivities for both magnetic field and temperature [29,30].

$$S(H) = \frac{\Delta\lambda_{peak}}{\Delta H_{Oe}}, \tag{8}$$

$$S(℃) = \frac{\Delta\lambda_{peak}}{\Delta T}, \tag{9}$$

Here, $\Delta\lambda_{peak}$ is peak wavelength differences. ΔH_{Oe} and ΔT are the external magnetic field and temperature variation, respectively. The obtained sensitivity was 12nm/Oe and 7.1nm/ºC for magnetic field and temperature. The acquired outcomes confirm that the proposed sensor can be manipulated for simultaneous measurement. The RI of the MF material is the role of temperature and the magnetic field change. The impact of this cross-sensitivity should not be ignored. Nevertheless, it should be involved in the description model of the sensor.

The figure of merit (FOM) is the key metric to assess the operation of any SPR sensor which can be evaluated using the following equation [31]

$$FOM = \frac{S_\lambda}{FWHM}, \tag{10}$$

where S_λ is the wavelength sensitivity determined in *nm/Oe* and FWHM is the full width at half maximum calculated in *nm* from the transmission intensity. Higher FOM signifies better sensing accuracy. Usually, a high-functioning sensor can be achieved when the sensitivity increases with a consistent decrease in FWHM. The highest figure of merit (FOM) is achieved as 665 Oe within the magnetic field range of 160 to 200 Oe. Similarly, another vital sensing factor is the resolution of a sensor that implies the smallest refractive index change or variation of sensing capacity. The resolution is identified as [32].

$$R(Oe) = \Delta H \frac{\Delta\lambda_{min}}{\Delta\lambda_{peak}}, \tag{11}$$

where ΔH indicates the alteration of external magnetic field strength, $\Delta\lambda_{min}$ shows the minimum difference between two peak wavelengths, and $\Delta\lambda_{peak}$ is the maximum peak wavelength shift. The maximum resolution was 5.53 Oe for the magnetic field strength of ΔH = 180 Oe, $\Delta\lambda_{min}$ = 0.06μm, and $\Delta\lambda_{peak}$ = 1.95μm. The proposed sensor will be crucial in the practical applications and in the advancement of optical sensing devices in a variety of contexts. Table 1 shows the comparison results of temperature and magnetic field sensitivity performances with those reported previously. This designed sensor has achieved the highest sensitivity performance with the highest detection range than previous work done.

Table 1. Comparatively results with the previous study.

Sensing structures	Materials	Wavelength (nm)	Range		Sensitivity		Ref.
			H	*T*	*H*	*T*	
Mach–Zehnder interferometer	Magnetic fluid	1520-1620	0-7 Gs	20-60ºC	0.72nm/Gs	-0.08nm/ºC	[33]
Temperature-insensitive magnetic field sensor	Magnetic fluid	1520-1600	0.01-2.03 KOe	30-100ºC	2.36pm/Oe	3.2pm/ºC	[34]
Fiber Bragg grating	Magnetic fluid	1540-1570	0-9 mT	15-45ºC	9.2pm/mT	11.9pm/ºC	[35]
Twin-core photonic crystal fiber	MF, silver, graphene	550-700	0-50 mT	20-50ºC	0.44nm/mT	-0.37nm/ºC	[36]
Whispering gallery modes in a photonic crystal fiber	Magnetic fluid	1520-1560	0-38 mT	-----	110pm/mT	-----	[37]
Novel nested anti-resonant fiber-based magnetic fluids	Magnetic fluid	600-1000	100-400 Oe	-----	6.8nm/Oe	-----	[38]
Plasmonic material and magnetic fluid-based PCF	MF, gold	1400-2000	160-200 Oe	25-100ºC	12nm/Oe	7.1nm/ºC	Proposed work

5. Conclusion

In conclusion, our work illustrates multi-parameter sensing by exploiting the highly refractive index sensing material. The photonic crystal fiber (PCF) based on coated plasmonic material and magnetic fluid (MF) filled into the core region is designed and studied to realize the simultaneous temperature and magnetic field measurement. The optical field scattering and loss spectra at different wavelengths are studied based on the COMSOL Multiphysics software by using the finite element method (FEM). The surface plasmon resonance (SPR) wavelength demonstrates high sensitivity due to the solid dispersion between the SPR attenuated modes

and the magnetic fluid. Temperature and magnetic field depend on the base of the MF refractive index. The sensitivity of the spectral reaction of the device to the magnetic field and temperature is considered. By tracing the peak wavelength shift, the achieved sensitivity was 12nm/Oe and 7.1nm/^{o}C for the magnetic field and temperature sensor, respectively. The achieved figure of merit (FOM) and resolution for the proposed sensor is 665 Oe and 5.53 Oe, respectively. Our investigated structure is presented with simplification and compactness to achieve better sensitivity. In this way, a new area of enhancement for combining the SPR and magnetic fluid is reviewed to develop the field of plasmonic-based technologies. The proposed sensor is straightforward, practical, and suitable for industries, security, small grids, and environmental applications. The formation can be further improved by alternating the parameters and sensing materials to obtain better results.

Disclosures. The authors declare that there is no conflict of interest.

Data availability. Data implicit in the results submitted in this report are not publicly accessible at this time but may be obtained from the authors upon reasonable request.

Funding: This research was funded by the Instituto Tecnológico y de Estudios Superiores de Monterrey (Tecnológico de Monterrey), N.L. 64849, México. This work is also partially supported by the funds of the DS Programs of Faculty of Electronics, Telecommunications, and Informatics of the Gdańsk University of Technology.

Acknowledgment: This research was supported by the Tecnológico de Monterrey, Monterrey, N.L. 64849, México. This work is also partially supported by the funds of the DS Programs of Faculty of Electronics, Telecommunications, and Informatics of the Gdańsk University of Technology, as well as of the funds of the National Science Centre, Poland [2021/41/N/ST7/03801].

References

1. M. I. A. Isti, H. Talukder, S. R. Islam, S. Nuzhat, A. S. Hosen, G. H. Cho, and S. K. Biswas, "Asymmetrical D-channel photonic crystal fiber-based plasmonic sensor using the wavelength interrogation and lower birefringence peak method," Results in Physics **19**, 103372 (2020).

2. E. Rodríguez-Schwendtner, N. Díaz-Herrera, M. C. Navarrete, A. González-Cano, and Ó. Esteban, "Plasmonic sensor based on tapered optical fibers and magnetic fluids for measuring magnetic fields," Sensors and Actuators A: Physical **264**, 58–62 (2017).

3. X. D. Wang, and O. S. Wolfbeis, "Fiber-Optic Chemical Sensors and Biosensors (2013-2015)," Analytical Chemistry **88**(1), 203–227 (2016).

4. H. Talukder, M. I. A. Isti, S. Nuzhat, and S. K. Biswas, "Ultra-High Negative Dispersion Based Single Mode Highly Nonlinear Bored Core Photonic Crystal Fiber (HNL-BCPCF): Design and Numerical Analysis," Brazilian Journal of Physics **50**(3), 263–270 (2020).

5. F. Haider, R. A. Ahmmed, R. Ahmed, W. J. Chew, and G. A. Mahdiraji, "Alphabetic-Core Assisted Microstructure Fiber Based Plasmonic Biosensor," Plasmonics **15**(6), 1949–1958 (2020).

6. K. M. Rahman, M. S. Alam, R. Ahmed, and M. A. Islam, "Irregular hexagonal core based surface plasmon resonance sensor in near-infrared region," Results in Physics **23**, 103983 (2021).

7. M. M. Bilal, W. Bi, X. Liu, L. Yang, J. Wa, and H. A. Madni, "Magnetic field sensor based on the magnetic fluid infiltration into the cladding air holes of the solid-core photonic crystal fiber," Optical Engineering **58**(9), 096107 (2019).

8. A. A. Nair, C. S. Boopathi, M. Jayaraju, and M. S. M. Rajan, "Numerical investigation and analysis of flattened dispersion for supercontinuum generation at very low power using hexagonal shaped photonic crystal fiber," Optik **179**, 718–725 (2019).

9. M. M. Rahman, M. M. Rana, M. S. Anower, M. S. Rahman, and A. K. Paul, "Design and analysis of photonic crystal fiber-based plasmonic microbiosensor: an external sensing scheme," SN Applied Sciences **2**(7), 1–11 (2020).

10. Y. Zhao, D. Wu, R. Q. Lv, and Y. Ying, "Tunable characteristics and mechanism analysis of the magnetic fluid refractive index with applied magnetic field," IEEE Transactions on Magnetics **50**(8), 1–5 (2014).

11. M. A. Mollah, S. M. R. Islam, M. Yousufali, L. F. Abdulrazak, M. B. Hossain, and I. S. Amiri, "Plasmonic temperature sensor using D-shaped photonic crystal fiber," Results in Physics **16**, 102966 (2020).

12. Y. Liu, X. Jing, S. Li, Y. Guo, S. Wang, J. Wang, and P. Yu, "High-sensitivity plasmonic temperature sensor based on gold-coated D-shaped photonic crystal fiber," Applied Optics **58**(18), 5115–5121 (2019).

13. Y. Peng, J. Hou, Z. Huang, and Q. Lu, "Temperature sensor based on surface plasmon resonance within selectively coated photonic crystal fiber," Appl. Opt. **51**(26), 6361–6367 (2012).

14. H. Liu, Y. Wang, C. Tan, C. Zhu, Y. Gao, H. Ma, and Z. Ren, "Simultaneous measurement of temperature and magnetic field based on cascaded photonic crystal fibers with surface plasmon resonance," Optik **134**, 257–263 (2017).

15. H. Liu, H. Li, Q. Wang, M. Wang, Y. Ding, and C. Zhu, "Simultaneous measurement of temperature and magnetic field based on surface plasmon resonance and Sagnac interference in a D-shaped photonic crystal fiber," Optical and Quantum Electronics **50**(11), 1–11 (2018).

16. Y. Chen, Q. Han, W. Yan, Y. Yao, and T. Liu, "Magnetic-fluid-coated photonic crystal fiber and FBG for magnetic field and temperature sensing," IEEE Photonics Technology Letters **28**(23), 2665–2668 (2016).

17. M. M. Rahman, M. M. Rana, M. S. Anower, M. S. Rahman, and A. K. Paul, "Design and analysis of photonic crystal fiber-based plasmonic microbiosensor: an external sensing scheme," SN Applied Sciences **2**(7), 1–11 (2020).

18. Q. M. Kamrunnahar, J. R.Mou, and M. Momtaj, "Dual-core gold coated photonic crystal fiber plasmonic sensor: Design and analysis," Results in Physics **18**, 103319 (2020).

19. F. Wei, A.K. Mallik, D. Liu, Q. Wu, G. D. Peng, and Y. Semenova, "Magnetic field sensor based on a combination of a microfiber coupler covered with magnetic fluid and a Sagnac loop," Scientific Reports **7**(1), 1–9 (2017).

20. S. A. Mitu, K. Ahmed, M. Hossain, B. K. Paul, T. K. Nguyen, and V. Dhasarathan, "Design of Magnetic Fluid Sensor Using Elliptically Hole Assisted Photonic Crystal Fiber (PCF)," Journal of Superconductivity and Novel Magnetism **33**(7), 2189–2198 (2020).

21. L. Zhao, H. Han, N. Luan, J. Liu, L. Song, and Y. Hu, "A temperature plasmonic sensor based on a side opening hollow fiber filled with high refractive index sensing medium," Sensors **19**(17), 3730 (2019).

22. K. Ahmed, M. A. Alzain, H. Abdullah, Y. Luo, D. Vigneswaran, O. S. Faragallah, M. Eid, and A. N. Z. Rashed, "Highly Sensitive Twin Resonance Coupling Refractive Index Sensor Based on Gold-and MgF 2-Coated Nano Metal Films," Biosensors (Basel) **11**(4), 104 (2021).

23. D. Vigneswaran, M. S. M. Rajan, B. Biswas, A. Grover, K. Ahmed, and B. K. Paul, "Numerical investigation of spiral photonic crystal fiber (S-PCF) with supporting high order OAM modes propagation for space division multiplexing applications," Optical and Quantum Electronics **53**(2), 1–11 (2021).

24. N. Ayyanar, D. Vigneswaran, M. Sharma, M. Sumathi, M. M. Rajan, and S. Konar, "Hydrostatic pressure sensor using high birefringence photonic crystal fibers," IEEE Sensors Journal **17**(3), 650–665 (2016).

25. M. Taghizadeh, F. Bozorgzadeh, and M .Ghorbani, "Designing magnetic field sensor based on tapered photonic crystal fibre assisted by a ferrofluid," Scientific Reports **11**(1), 1–9 (2021).

26. X. Bai, J. Yuan, J. Gu, S. Wang, Y. Zhao, and S. Pu, and X. Zeng, "Magnetic field sensor using fiber ring cavity laser based on magnetic fluid," IEEE Photonics Technology Letters **28**(2), 115–118 (2015).

27. K. Ahmed, M. Jabin, and B. K. Paul, "Surface plasmon resonance-based gold-coated biosensor for the detection of fuel adulteration," Journal of Computational Electronics **19**(1), 321–332 (2020).

28. M. A. Jabin, Y. Luo, G. D. Peng, M. J. Rana, K .Ahmed, T. K. Nguyen, and v. Dhasarathan, "Design and fabrication of amoeba faced photonic crystal fiber for biosensing application," Sensors and Actuators A: Physical **313**, 112204 (2020).

29. S. A. Mitu, K. Ahmed, M. Hossain, B. K. Paul, T. K. Nguyen, and v. Dhasarathan, "Design of Magnetic Fluid Sensor Using Elliptically Hole Assisted Photonic Crystal Fiber (PCF)," Journal of Superconductivity and Novel Magnetism **33**(7), 2189–2198 (2020).

30. Y. E. Monfared, C. Liang, R. Khosravi, B. Kacerovska, and S. Yang, "Selectively toluene-filled photonic crystal fiber Sagnac interferometer with high sensitivity for temperature sensing applications," Results in Physics **13**, 102297 (2019).

31. E. Haque, M. A. Hossain, and Y. Namihira, and F. Ahmed, "Microchannel-based plasmonic refractive index sensor for low refractive index detection," Appl. Opt. **58**(6), 1547–1554 (2019).

32. S. Zhang, W. Chen, H. Liu, Y. Ma, and M. Li, "Analysis of a magnetic field sensor based on photonic crystal fiber selectively infiltrated with magnetic fluids," Optical Fiber Technology **46**, 43–47 (2018).

33. X. G. Li, X. Zhou, Y. Zhao, and R. Q. Lv, "Multi-modes interferometer for magnetic field and temperature measurement using photonic crystal fiber filled with magnetic fluid," Optical Fiber Technology **41**, 1–6 (2018).

34. X. Zu, P. Chan, C. C. Lew, W. S. Hu, L. Jin, Y. Liew, H. F. Chen, L. H. Wong, and W. C. Dong, "Temperature-insensitive magnetic field sensor based on nanoparticle magnetic fluid and photonic crystal fiber," IEEE Photonics Journal **4**(2), 491–498 (2012).

35. C. Li, T. Ning, X. Wen, J. Li, and C. Zhang, "Magnetic field and temperature sensor based on a no-core fiber combined with a fiber Bragg grating," Optics & Laser Technology **72**, 104–107 (2015).

36. H. Liu, C. Chen, H. Wang, and W .Zhang, "Simultaneous measurement of magnetic field and temperature based on surface plasmon resonance in twin-core photonic crystal fiber," Optik **203**, 164007 (2020).

37. A. Mahmood, v .Kavungal, S. S .Ahmed, G. Farrell, and Y. Semenova, "Magnetic-field sensor based on whispering-gallery modes in a photonic crystal fiber infiltrated with magnetic fluid," Optics letters **40**(21), 4983–4986 (2015).

38. S. A. Mitu, K. Ahmed, F. M. Bui, P. Nithya, F. A. Al-Zahrani, M. A. Mollah, and M. M. Rajan, "Novel nested anti-resonant fiber based magnetic fluids sensor: Performance and bending effects inspection," Journal of Magnetism and Magnetic Materials **538**, 168230 (2021).